Finding Order in Disorder: The Highly Disordered Lithium Oxonitridophosphate Double Salt $Li_{8+x}P_3O_{10-x}N_{1+x}$ ($x = 1.4(5)$)

Stefanie Schneider,[a] Sandra T. Kreiner,[a] Lucas G. Balzat,[a, b] Bettina V. Lotsch,[a, b] and Wolfgang Schnick*[a]

Dedicated to Professor Michael Ruck on the occasion of his 60th Birthday.

The crystalline lithium oxonitridophosphate $Li_{8+x}P_3O_{10-x}N_{1+x}$, was obtained in an ampoule synthesis from P_3N_5 and Li_2O. The compound crystallizes in the triclinic space group $P\bar{1}$ with $a = 5.125(2)$, $b = 9.888(5)$, $c = 10.217(5)$ Å, $\alpha = 70.30(2)$, $\beta = 76.65(2)$, $\gamma = 77.89(2)°$. $Li_{8+x}P_3O_{10-x}N_{1+x}$ is a double salt, the structure of which contains distinctive complex anion species, namely non-condensed $P(O,N)_4$ tetrahedra, and $P(O,N)_7$ double tetrahedra connected by one N atom. Additionally, there is mixed occupation of O/N positions, which enables further anionic species by variation of O/N occupancies. To characterize these motifs in detail, complementary analytical methods were applied. The double tetrahedron exhibits significant disorder in single-crystal X-ray diffraction. Furthermore, the title compound is a Li^+ ion conductor with a total ionic conductivity of 1.2×10^{-7} S cm^{-1} at 25 °C, and a corresponding total activation energy of 0.47(2) eV.

Introduction

Lithium oxonitridophosphate (LiPON) glasses have been subject of extensive research since their discovery as Li^+ ion conductors in the 1990s.[1–5] Amorphous LiPON layers are deposited by sputtering Li_3PO_4 in a defined nitrogen-containing atmosphere.[1,2,6,7] Their electrochemical stability and ionic conductivity are much larger than that of the starting material and depend strongly on N-content and the atomic ratio of N/P.[6–9]

As solid state electrolyte, their mechanical stability enables the use of pure Li anodes, as dendrite formation during cycling is prevented.[10] Due to these properties and the easy formation of thin layers from inexpensive starting materials, amorphous LiPON has been used in thin film batteries of only several μm thickness.[2–5,11]

In spite of the comprehensive investigation of LiPON with spectroscopic methods, its missing long-range order made investigation of its structural intricacies impossible over a long period of time.[2,12–14] However, structural information is highly desirable in order to determine the correlation of structural with materials properties like ionic conductivity. Since common diffraction methods cannot be applied to amorphous materials, structural information must be obtained from short-range sensitive methods such as XPS, IR, or NMR.[2,14–16] However, owing to the sparse local structure information available, the structural traits of LiPON-type materials still remained largely speculative. The first crystalline lithium oxonitridophosphate $Li_{2.88}PO_{3.73}N_{0.14}$ enabled the complementary use of diffraction with short-range sensitive methods.[12,17] Thus, signals obtained from XPS and IR could be assigned to apical (N$_a$) or bridging (N$_b$) nitrogen atoms with the help of overall structural information from diffraction data. Since then, several further crystalline lithium oxonitridophosphates have been found that add to the pool of information on short-range sensitive data supported by long-range diffraction methods.[18–22]

Additionally, *in silico* methods like *ab initio* molecular dynamics (AIMD) simulations were employed to further characterize the structure of amorphous LiPON and its influence on conductivity.[9,12,23–25] It was observed that a high degree of disorder within the structure is beneficial for increased ionic conductivity due to flattened energy landscapes around Li^+ positions.[9,25]

Sharing various chemical and physical properties like chemical stability and physical hardness with amorphous LiPON, crystalline lithium oxonitridophosphates have also attracted notice as potential solid electrolytes to be used in all-solid-state batteries.[20] Furthermore, their structures exhibit significant

[a] S. Schneider, S. T. Kreiner, L. G. Balzat, Prof. Dr. B. V. Lotsch,
    Prof. Dr. W. Schnick
    Department of Chemistry
    University of Munich (LMU)
    Butenandtstraße 5–13 (D), 81377 Munich (Germany)
    E-mail: wolfgang.schnick@uni-muenchen.de

[b] L. G. Balzat, Prof. Dr. B. V. Lotsch
    Max Planck Institute for Solid State Research
    Department of Nanochemistry
    Heisenbergstraße 1 (D), 70569 Stuttgart (Germany)

Chem. Eur. J. **2023**, *29*, e202301986 (1 of 7)

© 2023 The Authors. Chemistry - A European Journal published by Wiley-VCH GmbH

Chemistry–A European Journal

Research Article
doi.org/10.1002/chem.202301986

Chemistry Europe
European Chemical
Societies Publishing

disorder. Whereas in Li_2PO_2N and $Li_{14}(PON_3)_2O$ full occupancy of O and N positions can be observed, $Li_{2.88}PO_{3.73}N_{0.14}$, $Li_{3.6}PO_{3.4}N_{0.6}$, $Li_{5+x}P_2O_{6-x}N_{1+x}$, and $Li_{27-x}[P_4O_{7+x}N_{9-x}]O_3$ exhibit mixed or partial occupancy of O and N positions.[17–22] This can lead to a significant degree of disorder and various different environments around Li. In these crystalline lithium oxonitridophosphates, different complex anions present in the structure are a result of mixed or statistical occupancy of O/N positions.[17,20,21] For example, mixed occupancy of O and N in $P(O,N)_4$ tetrahedra could result in PO_4, PO_3N, PO_2N_2, PON_3, and PN_4 motifs in the structure. In contrast, the structure of $Li_{8+x}P_3O_{10-x}N_{1+x}$ shows two different structural motifs, which are non-condensed tetrahedra and pairs of corner-sharing tetrahedra, both of which can have mixed occupancy of O/N positions. Since the distinction between O and N is difficult with X-ray diffraction, other analytical methods have to be employed. Solid-state magic-angle spinning (MAS) NMR spectroscopy is a powerful tool for the analysis of both crystalline and amorphous materials, as only the local environment is observed.[13,20,26–28] The different possible non-condensed $P(O,N)_4$ tetrahedra can be clearly distinguished, since the substitution of each O for N results in an additional shift of about $+10$ ppm.[13,20] Therefore, the structures of lithium oxonitridophosphates can only be distinguished by a combination of complementary analytical methods. In the case of $Li_{8+x}P_3O_{10-x}N_{1+x}$, the crystal structure was investigated by single-crystal X-ray diffraction, which allows the analysis of atomic positions, and by NMR, which allows the assignment of O and N occupancies to these sites in more detail. The characterization is complemented with IR and elemental analysis, thermal stability measurements, and the examination of ionic and electronic conductivity by impedance spectroscopy.

Results and Discussion

Synthesis

$Li_{8+x}P_3O_{10-x}N_{1+x}$ was obtained over a wide range in stoichiometry and reaction duration, by reaction of P_3N_5 with Li_2O in an open Ta crucible sealed under Ar into a silica ampoule. P_3N_5 and Li_2O in a molar ratio of 1:6 to 1:11 were heated to 800 °C with heating and cooling rates of 5 K min^{-1} and held for 30–90 h. Equation (1) shows the idealized reaction equation. An excess of Li_2O is beneficial for the formation of $Li_{8+x}P_3O_{10-x}N_{1+x}$ with as little $Li_{5+x}P_2O_{6-x}N_{1+x}$ side phase as possible. This corresponds well with other known lithium nitridophosphate and lithium oxonitridophosphate syntheses, in which an excess of lithium-containing starting material had to be used to acquire targeted compounds.[29–32] The formal formation of Li_3N has not been observed, possibly due to further reactions. Instead, small amounts of Li_3P were formed at elevated temperatures as has been observed in other lithium (oxo)nitridophosphate syntheses.[21,22,29–32] Li_3P was washed out with dry ethanol.

$$P_3N_5 + (10 - x)\, Li_2O \rightarrow Li_{8+x}P_3O_{10-x}N_{1+x} + (4 - x)\, Li_3N \qquad (1)$$
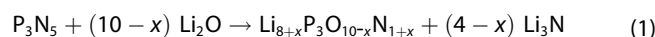
$Li_{8+x}P_3O_{10-x}N_{1+x}$ was obtained as colorless, microcrystalline powder sensitive to air and moisture. No phase pure synthesis could be achieved. Various amounts of Li_2O were present in all synthesis conditions and could not be avoided by variation of the amount of Li_2O as starting material. $Li_{5+x}P_2O_{6-x}N_{1+x}$ was another regularly observed side phase. Figure 1 shows the Rietveld refinement of a sample with the highest content of the targeted phase.

Crystal structure

The crystal structure of $Li_{8+x}P_3O_{10-x}N_{1+x}$ was determined by single-crystal X-ray diffraction. The structure crystallizes in the triclinic space group $P\bar{1}$ with $a = 5.125(2)$, $b = 9.888(5)$, $c = 10.217(5)$ Å, $\alpha = 70.30(2)$, $\beta = 76.65(2)$, $\gamma = 77.89(2)°$. Additional crystallographic details are listed in Table 1 and Tables S1–S4. The structure consists of $P(O,N)_4$ tetrahedra and pairs of tetrahedra $P_2(O,N)_7$ connected by one N atom, resulting in an oxonitridophosphate oxonitridodiphosphate (Figure 2a). NMR data suggest that P is coordinated by at least one N in both the non-condensed tetrahedron and the diphosphate motif. Due to the small X-ray scattering contrast and the large degree of disorder within this structure, exact positions of O and N cannot be assigned unequivocally. However, the obtained NMR data indicate occupation of bridging positions with N. As N atoms have been shown to be energetically favorable in contrast to O in bridging positions, this is considered accurate.[9,33,34] In the phosphate unit, N was placed according to ssNMR results and in positions that yielded a stable refinement and the best figures of merit. For a conclusive answer to the occupancy of O and N atoms, neutron diffraction would be required.

The non-condensed tetrahedron is slightly distorted. P–O/N bond lengths of 1.572(2)–1.592(3) Å are well within the range of known P–O and P–N distances in lithium phosphates[35–38] and
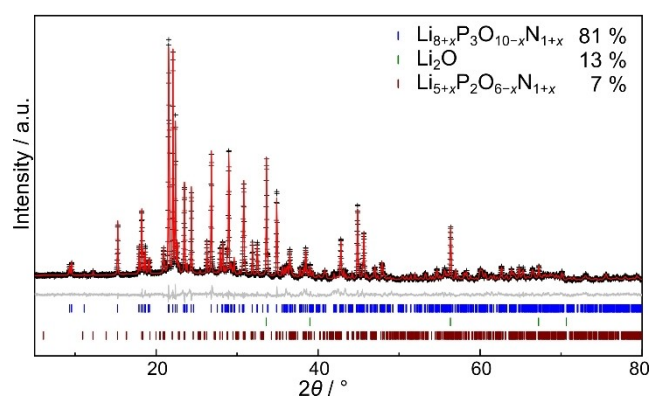
Figure 1. Rietveld Refinement for a sample of $Li_{8+x}P_3O_{10-x}N_{1+x}$ with measured (black crosses) and calculated (red) intensities and their difference (gray). The positions of reflections of $Li_{8+x}P_3O_{10-x}N_{1+x}$, Li_2O, and $Li_{5-x}P_2O_{6-x}N_{1+x}$ are shown with blue, green, and brown markers, respectively.

Chemistry–A European Journal

Research Article
doi.org/10.1002/chem.202301986

Chemistry Europe
European Chemical
Societies Publishing

Table 1. Crystallographic data on $Li_{8+x}P_3O_{10-x}N_{1+x}$.

Formula	$Li_{9.23}P_3O_{8.77}N_{2.23}$
Formula weight/g·mol^{-1}	328.54
Crystal system	triclinic
Space group	$P\bar{1}$ (no. 2)
Lattice parameters/Å, °	$a = 5.125(2)$
	$b = 9.888(5)$
	$c = 10.217(5)$
	$\alpha = 70.30(2)$
	$\beta = 76.65(2)$
	$\gamma = 77.89(2)$
Cell volume/Å^3	469.3(4)
Formula units per unit cell	2
Density/g·cm^{-3}	2.325
μ/mm^{-1}	0.673
Crystal size/mm^3	0.04×0.04×0.03
Radiation (λ/Å)	Mo-K$_\alpha$ $\lambda = 0.71073$ Å
θ-range/°	$3.522 \leq \theta \leq 18.995$
Total no. of reflections	12246
Independent reflections	3792, thereof 2748 with $F^2 > 2\sigma(F^2)$
Refined parameters	303
R_{int}; R_σ	0.0716; 0.0795
$R1$ (all data); $R1$ ($F^2 > 2\sigma(F^2)$)	0.0864; 0.0586
$wR2$ (all data); $wR2$ ($F^2 > 2\sigma(F^2)$)	0.1547; 0.1407
Goodness of fit (χ^2)	1.049
$\Delta\rho_{max}$; $\Delta\rho_{min}$/e·Å^{-3}	0.878; −0.992
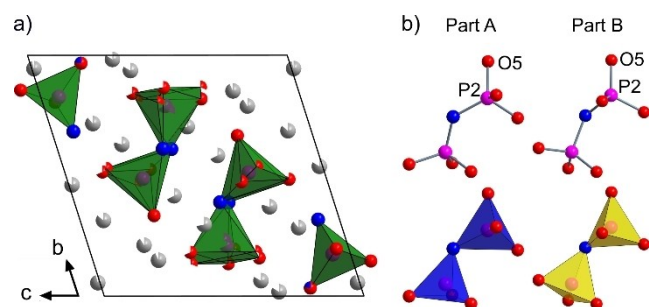
Figure 2. Structure of $Li_{8+x}P_3O_{10-x}N_{1+x}$. P and Li are shown in pink and gray, O and N in red and blue, respectively. a) Unit cell of $Li_{8+x}P_3O_{10-x}N_{1+x}$ along a with superimposed diphosphate motifs and their partial occupancies. Li positions were refined with an occupational restraint for charge neutrality. b) Side-by-side view of disordered diphosphate motifs as ball-and-stick representation (top) and as polyhedra (bottom). Rotation around the P2–O5 bond and tilting of the connected tetrahedron can project Part A onto Part B.

(oxo)nitridophosphates.[17–22,29–32] Angles within this tetrahedron range from 107.13(14)–114.84(14)°.

The diphosphate motif is highly disordered and can be explained with two orientations (Part A and Part B) that are twisted against each other around the P2–O5 bond and tilted in the bridging atom (Figure 2b). 31.5(8) % of O/N atoms occupy sites in Part A, whereas sites in Part B have an occupancy of 68.5(8) %. P–O/N distances in the diphosphate motif have a wider range compared to the non-condensed phosphate motif (1.568(3)–1.634(7) Å in Part A, 1.537(4)–

1.688(4) Å in Part B), which are, however, also well within the range of known P–O/N distances.[17–22,29—32,35–38] The P–N–P angle around P2–N08A–P03 A is with 130.5(11)° distinctly larger than that around P2–N08B–P03B (124.3(3)°) (Figure 2b). Presence of O or N at specific positions might influence preference of either Part A or Part B and influence occupancy of Li positions or vice versa.

There are eleven Li^+ positions found in the structure, all of which are not fully occupied when refined freely. Since free refinement does not yield charge neutrality, an occupancy restraint was used to match the anion charge and to produce a charge-neutral sum-formula. The Li positions exhibit very diverse, distorted coordination polyhedra (Figure S1). Neutron diffraction would provide more reliable data on the occupancy of Li positions.

Nuclear magnetic resonance (NMR) spectroscopy

Magic angle spinning (MAS) NMR spectra were obtained for ^{31}P, ^{6}Li, and ^{7}Li. The ^{31}P MAS NMR spectrum shows signals at 33.7, 21.8, and 16.3 ppm, with the signals at 21.8 and 16.3 ppm overlapping partly (Figure 3). From single-crystal X-ray diffraction the $P(O,N)_4$ and $P_2(O,N)_7$ motifs are expected in a 1:1 ratio. Thus, one third of the total area of the signals must result from non-condensed tetrahedra, whereas two thirds result from double-tetrahedra. The chemical shift of non-condensed $P(O,N)_4$ tetrahedra is well investigated and increases by about 10 ppm for each O that is substituted by N.[13,19,20,22,39] The signal at $\delta_{iso} = 33.7$ ppm can be assigned to $[PO_2N_2]^{5-}$, which is in good accordance with literature data (31.3 and 33.0 ppm).[20,22] The signal at 16.3 ppm is partly overlapped by the signal at 21.8 ppm, which results in a slight downfield-shift of the maximum upon comparison of the added signals with the deconvoluted signals. Deconvolution of the signals results in a maximum at 16.2 ppm. Overall, the chemical shift is in good
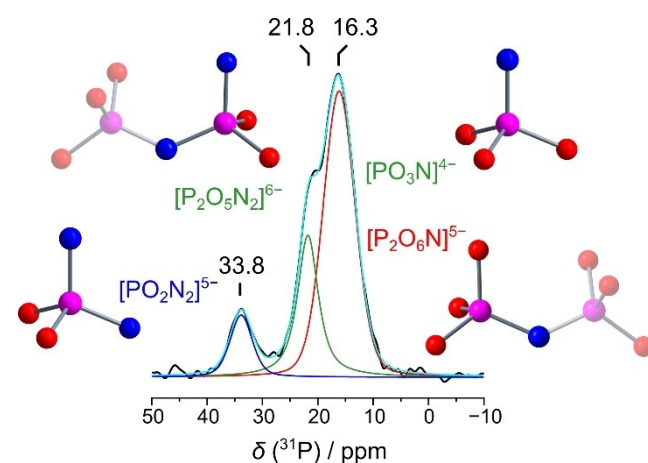
Figure 3. ^{31}P NMR spectrum with structural motifs corresponding to the respective signals. The signal at 33.8 ppm can be attributed to $[PO_2N_2]^{5-}$ (blue), the signal at 21.8 ppm is constituted from $[PO_3N]^{4-}$ and the doubly by N coordinated P in $[P_2O_5N_2]^{6-}$ (green), and the signal at 16.3 ppm results from the singly by N coordinated P in both $[P_2O_5N_2]^{6-}$ and $[P_2O_6N]^{5-}$ (red).

Chemistry–A European Journal

Research Article
doi.org/10.1002/chem.202301986

Chemistry Europe
European Chemical
Societies Publishing

agreement with $[P_2O_6N]^{5-}$ motifs in literature (14.6 and 14.2 ppm).[13,21] The signal resulting in a shoulder with a chemical shift of 21.8 ppm can be attributed either to $[PO_3N]^{4-}$ (19.4, 19.8, and 19.6 ppm in literature)[13,20,22] or to $[P_2O_5N_2]^{6-}$ (21.4 ppm in literature).[21] Deconvolution of the signals shows a 10.4(7):26.2(13):63(2) ratio. Since the signal at 33.8 ppm (10.4(7) % of the total area) can be assigned to $[PO_2N_2]^{5-}$ and one third of the overall signal area must result from non-condensed tetrahedra, another 22.9(7) % must result from $[PO_3N]^{4-}$, which is a large portion of the signal at 21.8 ppm. From this signal, which constitutes 26.2(13) % of the total area, 3.3(8) % remain. These 3.3(8) % of the total area result from the P coordinated by two N atoms within $[P_2O_5N_2]^{6-}$. As the bridging atom is assumed to be N, the diphosphate $[P_2O_6N_2]^{6-}$ must constitute the same amount from the remaining signal at 16.4 ppm. This signal at 16.4 ppm with 63(2) % of the total area results from singly N-coordinated P in both $[P_2O_6N]^{5-}$ (60(3) %) and $[P_2O_5N_2]^{6-}$ (3.3(8) %). In summary, the signal at 33.8 ppm stems from $[PO_2N_2]^{5-}$, the signal at 16.3 ppm is from the singly N-coordinated P within both diphosphate species ($[P_2O_5N_2]^{6-}$ and $[P_2O_6N]^{5-}$), and the signal at 21.8 ppm results from both $[PO_3N]^{4-}$ and the doubly N-coordinated P in $[P_2O_5N_2]^{6-}$. With this assignment of motifs, a sum formula of $Li_{9.4(14)}P_3O_{8.6(5)}N_{2.4(2)}$ results. Thus, the general sum formula $Li_{8+x}P_3O_{10-x}N_{1+x}$ can be obtained with $x = 1.4(5)$.

The ^6Li and ^7Li spectra each show one signal that cannot be deconvoluted (Figure S3). The width of the signal can be explained by the presence of eleven partly occupied Li positions, which are all slightly different. Due to the disorder in the diphosphate motif, coordination spheres around each Li position vary again, depending on which orientation of the diphosphate motif is coordinated. Only Li10 is coordinated solely by O and N from the phosphate motif, which does not exhibit disorder. Thus, Li10 exhibits only one coordination sphere (Figure S1).

Thermal stability measurements and FTIR spectroscopy

Variable-temperature powder X-ray diffraction of a sample with Li_2O as side phase showed additional reflections of $Li_{5+x}P_2O_{6-x}N_{1+x}$ and Li_3PO_4 above 720 °C due to decomposition of the title compound. Above 840 °C, mostly Li_3P remains (Figure 4).

Presence of hydrogen in the structure can be identified with infrared (IR) spectroscopy. O–H or N–H vibrations would be visible at around 2800–3200 or 3000–3500 cm^{-1}, respectively.[40–42] As no such signal is present in these areas, the presence of H in the structure can be excluded (Figure 5). P–O and P–N vibrational bands are visible in the fingerprint area between 400–1200 cm^{-1}. However, the signals are superimposed and cannot be resolved and assigned to distinct vibrations.
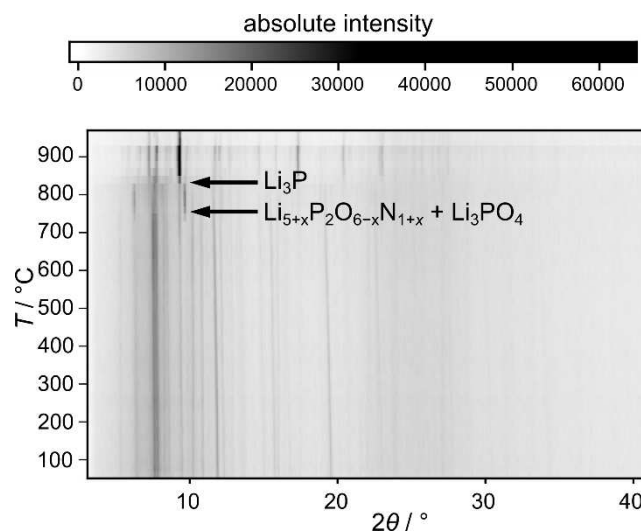

Figure 4. Variable-temperature powder X-ray diffraction measurement of $Li_{8+x}P_3O_{10-x}N_{1+x}$ from 60–960 °C.

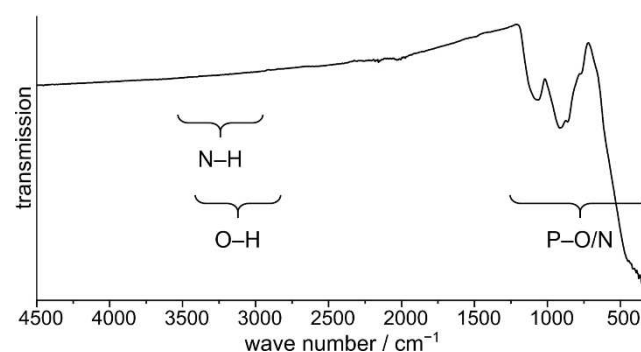**Figure 5.** Infrared transmission spectrum of $Li_{8+x}P_3O_{10-x}N_{1+x}$ measured under Ar with an ATR unit with diamond window.
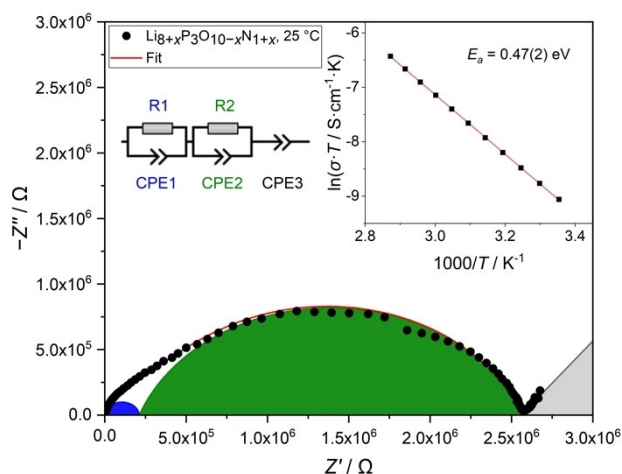
Elemental analysis

Energy-dispersive X-ray spectroscopy showed a very large deviation from calculated values as obtained from NMR ($x = 1.4$). Instead, EDX suggests a stoichiometry of $Li_{11}P_3O_7N_4$ ($x = 3$) (Table S6). However, the uncertainties of these values are very large due to the presence of light atoms. The sum formula derived from EDX would be $Li_{11(8)}P_{3.0(13)}O_{7(5)}N_{4(2)}$.

The N content measured with CHNS is slightly larger than expected for $Li_{8+x}P_3O_{10-x}N_{1+x}$. The side phase $Li_{5+x}P_2O_{6-x}N_{1+x}$ was considered in the calculations with an average value of $x = 0.9$. However, as this phase is not stoichiometrically precise, the deviation of the measured from the expected value might be increased by the coexistence of this side phase.

Ionic and electronic conductivity measurements

The ionic conductivity of $Li_{8+x}P_3O_{10-x}N_{1+x}$ was determined by electrochemical impedance spectroscopy (EIS). Figure 6 shows EIS data gathered from a pellet containing 70 wt.% $Li_{8+x}P_3O_{10-x}N_{1+x}$, 24 wt.% Li_2O and 6 wt.% $Li_{5+x}P_2O_{6-x}N_{1+x}$ (phase composi-

Chemistry–A European Journal

Research Article
doi.org/10.1002/chem.202301986

Chemistry Europe
European Chemical
Societies Publishing

Figure 6. Nyquist plot of impedance data of $Li_{8+x}P_3O_{10-x}N_{1+x}$ gathered at 25 °C. The contributions of the first (R1/CPE1; blue) and second semicircle (R2/CPE2, green) are highlighted, respectively. The inset shows an Arrhenius plot of temperature-dependent EIS data, resulting in a total activation energy of $E_a = 0.47(2)$ eV.

tion determined from Rietveld refinement). Three processes are visible, indicated as two semicircles and one spike in the low-frequency range. The semicircles were modeled with a serial connection of a resistor (R) and a constant phase element (CPE) in parallel, while the low-frequency polarization spike was modeled with an additional CPE in series. CPEs were chosen to account for non-ideal sample behavior.[43] To assign processes to the semicircles, the capacities of CPE1 and CPE2 were calculated using the Brug formula.[44] At 25 °C the first and second semicircle exhibit capacities of 1.7×10^{-11} F and 3.8×10^{-11} F, respectively. Because the capacities are very similar it is not possible to assign bulk and grain boundary contributions to the individual semicircles.[45] Therefore, in the following only the total conductivity and total activation energy are reported.

Using R1 + R2 the total ionic conductivity is found to be 1.2×10^{-7} S cm^{-1} at 25 °C. The total activation energy of $Li_{8+x}P_3O_{10-x}N_{1+x}$ was determined by fitting temperature dependent EIS data to a linear Arrhenius-type behavior, resulting in a total activation energy of 0.47(2) eV (see inset Figure 6).

The electronic conductivity of $Li_{8+x}P_3O_{10-x}N_{1+x}$ was determined via potentiostatic polarization measurements. An exemplary U-I curve is displayed in Figure S5. $Li_{8+x}P_3O_{10-x}N_{1+x}$ shows an electronic conductivity of 2.3×10^{-9} S cm^{-1} at 25 °C, about two orders of magnitude lower than its ionic conductivity. With an ionic transference number $\tau_i = \sigma_{ion}/(\sigma_{ion} + \sigma_{eon})$ of 0.981, $Li_{8+x}P_3O_{10-x}N_{1+x}$ can thus be classified as a predominantly ionic conductor with a small, yet significant electronic conductivity.

Since only multi-phase samples of $Li_{8+x}P_3O_{10-x}N_{1+x}$ in small quantities were available, several EIS measurements using two samples with different compositions were carried out to ensure reproducibility (see Supporting Information and Figure S4 for a discussion on reproducibility). Generally, the total conductivities of the two measured samples vary slightly (1.2×10^{-7} S cm^{-1} and 3.4×10^{-8} S cm^{-1}, 25 °C), which is likely due to differing phase

compositions, while the total activation energies are in good agreement. The ionic conductivity of $Li_{8+x}P_3O_{10-x}N_{1+x}$ is comparable to that of other known lithium oxonitridophosphates, which range from 1×10^{-13} S cm^{-1} ($Li_{2.88}PO_{3.73}N_{0.14}$) to 1.6×10^{-6} S cm^{-1} (amorphous LiPON) at room temperature.[17,18,20–22,46]

Conclusions

With $Li_{8+x}P_3O_{10-x}N_{1+x}$, a new crystalline lithium oxonitridophosphate was synthesized from ampoule synthesis. It is a double salt containing both phosphate and diphosphate motifs. With mixed occupancies, as shown by NMR spectroscopy, the following structural motifs could be identified: PO_2N_2, PO_3N, P_2O_6N, and $P_2O_5N_2$. Furthermore, the diphosphate motif exhibits severe disorder. For further characterization and more detailed information on both O/N and Li occupancy, neutron diffraction would be indispensable. Impedance spectroscopy showed a total Li$^+$ conductivity of 1.2×10^{-7} S cm^{-1} at 25 °C, with a total activation energy of 0.47(2) eV, which is within the range of other crystalline lithium oxonitridophosphates.[17,18,20–22,46] The significant disorder in the structure might be beneficial for the system's conductivity. Density functional theory (DFT) calculations could be employed to give further insights to the mechanisms of conductivity in lithium oxonitridophosphates in general and in $Li_{8+x}P_3O_{10-x}N_{1+x}$ specifically.

If applied as thin film, the conductivity of $Li_{8+x}P_3O_{10-x}N_{1+x}$ might be sufficient for use in thin film batteries. Thus, its applicability as electrolyte against suitable electrode materials should be investigated, as the electrochemical stability window, stability against reaction with Li, and cycle stability are not yet known. Considering the immense structural diversity of lithium nitridophosphates and the few hitherto known lithium oxonitridophosphates, lithium oxonitridophosphates harbor the potential of a large amount of complex crystal structures, some of which might exhibit much larger ionic conductivities than the known representatives.

Experimental Section

Synthesis of P_3N_5:[47] P_4S_{10} (Acros Organics, >99.8%) was placed into a dried silica tube within a silica reaction tube in Ar (Air Liquide, 99.999%) counterflow. After saturation with NH$_3$ (Air Liquide, 99.999%) over 4 h, the starting material was heated to 850 °C at 5 K min^{-1} and held for 4 h before cooling at −5 K min^{-1}. The orange product was removed and washed with diluted hydrochloric acid, water, and acetone.

Synthesis of $Li_{8+x}P_3O_{10-x}N_{1+x}$: P_3N_5, and Li_2O (molar ratio 1:9) were ground together in an argon-filled glovebox (Unilab, MBraun, Garching, $O_2 < 1$ ppm, $H_2O < 1$ ppm), transferred in Ar counterflow into a Ta crucible within a silica tube and sealed into a silica ampoule under Ar. The mixture was heated to 800 °C at a rate of 5 K min^{-1}, held for 90 h and cooled at a rate of 5 K min^{-1}. The air-sensitive product was obtained as off-white powder under Ar.

Single-crystal X-ray diffraction: Single crystals were chosen under dried paraffin oil and irradiated with Mo-K$_\alpha$ radiation ($\lambda = 0.71073$ Å) from a rotating anode in a D8 Venture (Bruker, Billerica MA, USA). Absorption correction was performed with SADABS and integration

was performed with the APEX 3 program package.[48,49] The structure was solved with SHELXT and refined with SHELXL.[50]

Deposition Numbers 2246044 contain the supplementary crystallographic data for this paper. These data are provided free of charge by the joint Cambridge Crystallographic Data Centre and Fachinformationszentrum Karlsruhe Access Structures service.

X-ray powder diffraction: Glass capillaries (diameter 0.5 mm, wall thickness 0.01 mm, Hilgenberg GmbH) filled to ca. 1.5 cm, sealed off and mounted on a Stoe STADI P diffractometer. The sample was irradiated with Cu-K$_{\alpha 1}$ radiation ($\lambda = 1.5406$ Å) through a Ge(111) monochromator. Data was obtained with a Mythen 1 K detector in Debye–Scherrer geometry.

Temperature-dependent powder X-ray diffraction data was obtained on a Stoe StadiP equipped with a graphite furnace and an imaging plate position sensitive detector. The sample was irradiated with Ag-K$_{\alpha 1}$ radiation ($\lambda = 0.5594075$ Å) with a Ge(111) monochromator. The sample was filled into a quartz glass capillary (diameter 0.4 mm, wall thickness 0.01 mm, Hilgenberg GmbH) and closed with a clog of vacuum grease (Leybonol, LVO 810 Lithelen). Measurements were taken from 60–960 °C in steps of 20 K, with a heating rate of 5 K min^{-1}.

Solid-state magic angle spinning (MAS) NMR methods: A DSX AVANCE spectrometer (Bruker) with a magnetic field of 11.7 T was used to collect NMR spectra of ^{6}Li, ^{7}Li, and ^{31}P. Li$_{8+x}$P$_3$O$_{10-x}$N$_{1+x}$ was filled into a rotor ($\varnothing = 2.5$ mm), which was then spun with a rotation frequency of 20 kHz on a commercial MAS probe (Bruker). The spectra were analyzed using device-specific software.[51]

Fourier-transform Infrared (FTIR) spectroscopy: FTIR data was obtained using a Bruker FTIR Alpha II compact spectrometer with a diamond ATR unit under Ar atmosphere. The spectrum was measured from 400–4000 cm^{-1}.

Elemental analysis: Energy-dispersive X-ray spectroscopy (EDX): A scanning electron microscope (Dualbeam Helios Nanolab G3 UC (FEI)) equipped with an EDX detector (X–Max 80 SDD, Oxford Instruments) was used for EDX measurements. The samples were positioned on adhesive carbon pads and coated with a conductive carbon film using a high-vacuum sputter coater (safematic CCU-010). Using an accelerating voltage of 20 kV, multiple particles were targeted.

Inductively coupled plasma optical emission spectrometry (ICP-OES): ICP-OES was conducted at a Varian Vista RL with a 40 MHz RF generator, and a CCD detector (VistaChip).

Mass spectrometry: CHNS spectrometry was performed on a Vario MICRO Cube device (Elementar, Langenselbold, Germany).

Electrochemical measurements: Before the measurements, the samples were thoroughly ground in an agate mortar and then compacted into pellets of approximately 0.3–0.7 mm thickness and 5 mm in diameter using uniaxial cold-pressing (p $\approx$ 2 t). The pellets were then sputtered with platinum metal using a Quorum 150 GB sputter coater to achieve an ion-blocking measurement setup and to ensure good contact during measurements. The ionic conductivity was determined via EIS, which was carried out in a two-electrode setup using an Ivium compactstat.h potentiostat (24 bit instrument) with a RHD Instruments Microcell HC cell stand loaded with a RHD Instruments TSC SW Closed measuring cell. All samples were measured in the frequency range of 1 MHz–0.1 Hz with an excitation voltage of 100 mV. The applied pressure in the measuring cells was about 700 kPa.

The activation energy was determined by fitting temperature dependent data to a linear Arrhenius-type behavior. Temperature-dependent data were collected between 25–75 °C in 5 K steps and

an equilibration time of 1 h was used. Data analysis and fitting procedures of EIS data were carried out using the software RelaxIS 3 (RHD Instruments, Darmstadt).

After EIS measurements, the pellets were kept in the same measurement cells and were subsequently used for the determination of the electronic conductivity. The electronic conductivity was determined via potentiostatic polarization measurements at 25 °C. Voltages of 0.25, 0.50, 0.75, 1.00 and 1.25 V were applied for 16 h each with the drop of the resulting current measured. The resistance was extracted using Ohm's law from the current measured at a steady state after 16 h.

Sample preparation and electrochemical measurements were carried out in an argon-filled glovebox (MB200, MBraun, Garching, O$_2$ < 0.1 ppm, H$_2$O < 0.1 ppm).

Supporting Information

The authors have cited additional references within the Supporting Information.[52–58]

Conflict of Interests

The authors declare no conflict of interest.

Data Availability Statement

The data that support the findings of this study are available in the supplementary material of this article.

[1] J. B. Bates, N. J. Dudney, G. R. Gruzalski, R. A. Zuhr, A. Choudhury, C. F. Luck, J. D. Robertson, *Solid State Ionics* **1992**, *53*, 647–654.
[2] J. B. Bates, N. J. Dudney, G. R. Gruzalski, R. A. Zuhr, A. Choudhury, C. F. Luck, J. D. Robertson, *J. Power Sources* **1993**, *43*, 103–110.
[3] J. B. Bates, G. R. Gruzalski, N. J. Dudney, C. F. Luck, X. Yu, *Solid State Ionics* **1994**, *70–71*, 619–628.
[4] J. B. Bates, N. J. Dudney, D. C. Lubben, G. R. Gruzalski, B. S. Kwak, X. Yu, R. A. Zuhr, *J. Power Sources* **1995**, *54*, 58–62.
[5] J. B. Bates, N. J. Dudney, B. Neudecker, A. Ueda, C. D. Evans, *Solid State Ionics* **2000**, *135*, 33–45.

Chemistry–A European Journal

Research Article
doi.org/10.1002/chem.202301986

Chemistry
Europe
European Chemical
Societies Publishing

[6] Y. Hamon, A. Douard, F. Sabary, C. Marcel, P. Vinatier, B. Pecquenard, A. Levasseur, *Solid State Ionics* **2006**, *177*, 257–261.

[7] H. Y. Park, S. C. Nam, Y. C. Lim, K. G. Choi, K. C. Lee, G. B. Park, S. R. Lee, H. P. Kim, S. B. Cho, *J. Electroceram.* **2006**, *17*, 1023–1030.

[8] X. Yu, J. B. Bates, G. E. Jellison, F. X. Hart, *J. Electrochem. Soc.* **1997**, *144*, 524–532.

[9] V. Lacivita, N. Artrith, G. Ceder, *Chem. Mater.* **2018**, *30*, 7077–7090.

[10] E. G. Herbert, W. E. Tenhaeff, N. J. Dudney, G. M. Pharr, *Thin Solid Films* **2011**, *520*, 413–418.

[11] S. D. Jones, J. R. Akridge, F. K. Shokoohi, *Solid State Ionics* **1994**, *69*, 357–368.

[12] V. Lacivita, A. S. Westover, A. Kercher, N. D. Phillip, G. Yang, G. Veith, G. Ceder, N. J. Dudney, *J. Am. Chem. Soc.* **2018**, *140*, 11029–11038.

[13] M. A. T. Marple, T. A. Wynn, D. Cheng, R. Shimizu, H. E. Mason, Y. S. Meng, *Angew. Chem. Int. Ed.* **2020**, *59*, 22185–22193; *Angew. Chem.* **2020**, *132*, 22369–22377.

[14] M. A. Carrillo Solano, M. Dussauze, P. Vinatier, L. Croguennec, E. I. Kamitsos, R. Hausbrand, W. Jaegermann, *Ionics* **2016**, *22*, 471–481.

[15] B. C. Bunker, D. R. Tallant, C. A. Balfe, R. J. Kirkpatrick, G. L. Turner, M. R. Reidmeyer, *J. Am. Ceram. Soc.* **1987**, *70*, 675–681.

[16] B. Fleutot, B. Pecquenard, H. Martinez, M. Letellier, A. Levasseur, *Solid State Ionics* **2011**, *186*, 29–36.

[17] B. Wang, B. C. Chakoumakos, B. C. Sales, B. S. Kwak, J. B. Bates, *J. Solid State Chem.* **1995**, *115*, 313–323.

[18] K. Senevirathne, C. S. Day, M. D. Gross, A. Lachgar, N. A. W. Holzwarth, *Solid State Ionics* **2013**, *233*, 95–101.

[19] D. Baumann, W. Schnick, *Eur. J. Inorg. Chem.* **2015**, 617–621.

[20] P. López-Aranguren, M. Reynaud, P. Głuchowski, A. Bustinza, M. Galceran, J. M. López Del Amo, M. Armand, M. Casas-Cabanas, *ACS Energy Lett.* **2021**, *6*, 445–450.

[21] S. Schneider, L. G. Balzat, B. V. Lotsch, W. Schnick, *Chem. Eur. J.* **2023**, *29*, 10.1002/chem.202202984.

[22] S. Schneider, E.-M. Wendinger, V. Baran, A.-K. Hatz, B. V. Lotsch, M. Nentwig, O. Oeckler, T. Bräuniger, W. Schnick, *Chem. Eur. J.* **2023**, *29*, 10.1002/chem.202300174.

[23] H. Rabaâ, R. Hoffmann, N. Cruz Hernández, J. Fernandez Sanz, *J. Solid State Chem.* **2001**, *161*, 73–79.

[24] N. D. Lepley, N. A. W. Holzwarth, *J. Electrochem. Soc.* **2012**, *159*, A538-A547.

[25] J. Li, W. Lai, *Solid State Ionics* **2020**, *351*, 115329.

[26] G. L. Paraschiv, F. Muñoz, L. R. Jensen, Y. Yue, M. M. Smedskjaer, *J. Am. Ceram. Soc.* **2018**, *101*, 5004–5019.

[27] A. Kidari, C. Mercier, A. Leriche, B. Revel, M. J. Pomeroy, S. Hampshire, *Mater. Lett.* **2012**, *84*, 38–40.

[28] N. Mascaraque, J. L. G. Fierro, F. Muñoz, A. Durán, Y. Ito, Y. Hibi, R. Harada, A. Kato, A. Hayashi, M. Tatsumisago, *J. Mater. Res.* **2015**, *30*, 2940–2948.

[29] E.-M. Bertschler, R. Niklaus, W. Schnick, *Chem. Eur. J.* **2017**, *23*, 9592–9599.

[30] E.-M. Bertschler, C. Dietrich, J. Janek, W. Schnick, *Chem. Eur. J.* **2017**, *23*, 2185–2191.

[31] E.-M. Bertschler, C. Dietrich, T. Leichtweiß, J. Janek, W. Schnick, *Chem. Eur. J.* **2018**, *24*, 196–205.

[32] E.-M. Bertschler, R. Niklaus, W. Schnick, *Chem. Eur. J.* **2018**, *24*, 736–742.

[33] Y. A. Du, N. A. W. Holzwarth, *Phys. Rev. B* **2010**, *81*, 1–15.

[34] Y. A. Du, N. A. W. Holzwarth, *Phys. Rev. B* **2008**, *78*, 1–13.

[35] N. I. P. Ayu, E. Kartini, L. D. Prayogi, M. Faisal, Supardi, *Ionics* **2016**, *22*, 1051–1057.

[36] V. I. Voronin, E. A. Sherstobitova, V. A. Blatov, G. S. Shekhtman, *J. Solid State Chem.* **2014**, *211*, 170–175.

[37] B. Raguž, K. Wittich, R. Glaum, *Eur. J. Inorg. Chem.* **2019**, *2019*, 1688–1696.

[38] T. Ben-Chaabane, L. Smiri-Dogguy, Y. Laligant, A. Le Bail, *Eur. J. Solid State Inorg. Chem.* **1998**, *35*, 255–264.

[39] E.-M. Bertschler, Novel Lithium Nitridophosphates and Their Capability as Lithium Ion Conductors, Ludwig-Maximilians-University Munich, **2017**.

[40] W. Schnick, J. Lücke, *Z. Anorg. Allg. Chem.* **1992**, *610*, 121–126.

[41] S. Horstmann, E. Irran, W. Schnick, *Z. Anorg. Allg. Chem.* **1998**, *624*, 620–628.

[42] D. Baumann, W. Schnick, *Inorg. Chem.* **2014**, *53*, 7977–7982.

[43] J. R. Macdonald, W. B. Johnson, in *Impedance Spectroscopy: Theory, Experiment, and Applications, Second Edition*, John Wiley & Sons, Inc., Hoboken, NJ, **2005**, pp. 1–26.

[44] G. J. Brug, A. L. G. van den Eeden, M. Sluyters-Rehbach, J. H. Sluyters, *J. Electroanal. Chem.* **1984**, *176*, 275–295.

[45] J. T. S. Irvine, D. C. Sinclair, A. R. West, *Adv. Mater.* **1990**, *2*, 132–138.

[46] S. Zhao, Z. Fu, Q. Qin, *Thin Solid Films* **2002**, *415*, 108–113.

[47] A. Stock, B. Hoffmann, *Ber. Dtsch. Chem. Ges.* **1903**, *36*, 314–319.

[48] Bruker, *SADABS*, Bruker AXS Inc., Madison, WI, USA, **2009**.

[49] Bruker, *APEX3 V2018.1-0*, **2018**.

[50] G. M. Sheldrick, *Acta Crystallogr. Sect. C* **2015**, *71*, 3–8.

[51] Bruker, *Topspin v.3.0 Pl 3*, Bruker Biospin GmbH, Germany, **2010**.

[52] E.-M. Bertschler, T. Bräuniger, C. Dietrich, J. Janek, W. Schnick, *Angew. Chem. Int. Ed.* **2017**, *56*, 4806–4809; *Angew. Chem.* **2017**, *129*, 4884–4887.

[53] R. Böhmer, K. R. Jeffrey, M. Vogel, *Prog. Nucl. Magn. Reson. Spectrosc.* **2007**, *50*, 87–174.

[54] A. Kuhn, V. Duppel, B. V. Lotsch, *Energy Environ. Sci.* **2013**, *6*, 3548–3552.

[55] R. W. Cheary, A. A. Coelho, *J. Appl. Crystallogr.* **1992**, *25*, 109–121.

[56] R. W. Cheary, A. A. Coelho, J. P. Cline, *J. Res. Natl. Inst. Stan.* **2004**, *109*, 1–25.

[57] A. A. Coelho, *TOPAS Academic Version 6*, Coelho Software, Brisbane, Australia, **2016**.

[58] S. Lorger, R. Usiskin, J. Maier, *J. Electrochem. Soc.* **2019**, *166*, A2215-A2220.